CrystEngComm

PAPER

View Article Online
View Journal | View Issue

Cite this: *CrystEngComm*, 2014, **16**, 344

Photoluminescent layered lanthanide–organic framework based on a novel trifluorotriphosphonate organic linker†

Sérgio M. F. Vilela,[ab] José A. Fernandes,[a] Duarte Ananias,[a] Luís D. Carlos,[c] João Rocha,[a] João P. C. Tomé[b] and Filipe A. Almeida Paz*[a]

Received 26th July 2013,
Accepted 12th October 2013

DOI: 10.1039/c3ce41482e

www.rsc.org/crystengcomm

A series of fluorinated lanthanide–organic frameworks (LnOFs), formulated as [Ln(**H$_3$tftp**)(H$_2$O)] [where Ln^{3+} = La^{3+} (**1**), (La$_{0.95}$Eu$_{0.05}$)$^{3+}$ (**2**), (La$_{0.95}$Tb$_{0.05}$)$^{3+}$ (**3**) and (La$_{0.94}$Eu$_{0.03}$Tb$_{0.03}$)$^{3+}$ (**4**)], has been successfully prepared, under hydrothermal conditions, using the novel ((2,4,6-trifluorobenzene-1,3,5-triyl)tris (methylene))triphosphonic acid (**H$_6$tftp**) organic ligand and Ln^{3+} cations as metallic centers. The three-step preparation of the tripodal **H$_6$tftp** ligand is described. **H$_6$tftp** and all intermediate molecules involved in the synthesis were fully characterized in the liquid and solid states. While the La^{3+}-based LnOF material was isolated as single-crystals, with its crystal structure being fully described by single-crystal X-ray diffraction, phase identification of the Eu^{3+}- and Tb^{3+}-based materials was performed by powder X-ray diffraction. It is shown that the crystal structure of this isotypical series of materials is based on a neutral two-dimensional $_{\infty}^{2}$[Ln(**H$_3$tftp**)(H$_2$O)] coordination polymer placed in the *ac* plane of the unit cell, exhibiting a uninodal 4-connected square layered topology. It is shown that the most striking and supramolecular relevant interactions are classical O–H···O hydrogen bonds within the polymer, further contributing to the structural robustness of the layer. Prepared LnOFs were fully characterized in the solid state using elemental and thermogravimetric analysis, electron microscopy (SEM and EDS) and FT-IR spectroscopy. Compound **1** was further studied using solid-state NMR (^{31}P HPDEC MAS and ^{13}C{^{1}H} CP MAS) and thermodiffractometry. Photoluminescent studies have been performed on the mixed-lanthanide materials **2** and **3**.

1. Introduction

Considerable worldwide efforts have been focused in the design and preparation of multidimensional and functional hybrid materials designated as coordination polymers, or frequently also known as metal–organic frameworks (MOFs).[1] These compounds are prepared from the self-assembly between metallic centers and multitopic organic ligands, leading in many circumstances to intriguing architectures with unique properties. MOFs have found potential applications in very distinct fields of science ranging from gas storage and separation,[2] ion exchange,[2g,3] catalysis,[4] magnetism,[5] as optical sensors,[4b,6] to imaging contrast agents,[7] among many others.

A careful selection of the synthetic methods and of the primary building units (PBUs: *i.e.*, metallic centers and organic ligands) is of crucial importance toward designing robust novel and functional architectures. Although not very common, perfluorinated or partially fluorinated organic linkers in which the hydrogen atoms are replaced by fluorine or –CF$_3$ groups have already been used in the preparation of functional MOFs. Compared with non-fluorinated, fluorinated MOFs have shown to enhance the hydrophobicity, increase structural stability in water or moisture atmospheres, and even to improve the photoluminescent properties.[8] Additionally, the presence of fluorine atoms as constituents of the organic molecules may lead to the formation of F···F interactions, helping to stabilize the resulting networks.[9]

Fully or partially fluorinated MOFs have been studied, mainly, as potential materials for application in adsorption processes,[10] and luminescent devices.[11] Omary and co-workers have reported the synthesis of totally fluorinated MOFs, coined as FMOF-1 and FMOF-2, from the combination of Ag^{+} with the 3,5-bis(trifluoromethyl)-1,2,4-triazolate organic ligand.[8c,12] The hydrophobicity of FMOF-1 is the main characteristic responsible for the observed efficient selective adsorption ability of aliphatic and aromatic oil components (benzene, toluene, *p*-xylene, cyclohexane and *n*-hexane), while preventing the entrance of water molecules in their pores. Chen *et al.* have isolated two Er^{3+}–

[a] *Department of Chemistry, CICECO, University of Aveiro, 3810-193 Aveiro, Portugal. E-mail: filipe.paz@ua.pt; Fax: +351 234 370 084; Tel: +351 234 247 126*
[b] *Department of Chemistry, QOPNA, University of Aveiro, 3810-193 Aveiro, Portugal*
[c] *Department of Physics, CICECO, University of Aveiro, 3810-193 Aveiro, Portugal*

† Electronic supplementary information (ESI) available. CCDC 952452–952455. For ESI and crystallographic data in CIF or other electronic format see DOI: 10.1039/c3ce41482e

organic frameworks, $[Er_2(bdc)_3(DMF)_2(H_2O)_2]\cdot H_2O$ and $[Er_2(bdc\text{-}F_4)_3(DMF)(H_2O)]\cdot DMF$, by using the organic linkers 1,4-benzenedicarboxylate (H_2bdc) and its fluorinated analogue 2,3,5,6-tetrafluoro-1,4-benzenedicarboxylate ($H_2bdc\text{-}F_4$), respectively.[11a] In this comparative study the authors showed that the replacement of the C–H fluorescence quencher by C–F groups improves significantly (approximately three times) the near-IR-luminescence intensity. We note that the use of fluorinated organic molecules does not, however, ensure just by itself an improvement in the desired properties of the resulting material. A striking example concerns the work reported by Banerjee's group on a handful of fluorinated and nonfluorinated MOFs, showing that it is difficult to evaluate the influence of fluorination on H_2 and CO_2 adsorption.[13]

Optically-active lanthanide- (or mixed-lanthanide-) based compounds have found potential applications in the fabrication of sensing devices.[14] In recent years we have focused our research efforts in the preparation of multidimensional and functional lanthanide–organic frameworks (LnOFs) based on phosphonate organic linkers.[15] Following our interest in the design and synthesis of novel organic ligands,[16] we have designed and prepared (in a three-step reaction) the novel fluorinated tripodal organic ligand ((2,4,6-trifluorobenzene-1,3,5-triyl)tris(methylene))triphosphonic acid (H_6tftp). This molecule is a structural analogue of the previously reported (benzene-1,3,5-triyl)tris(methylene)triphosphonic acid (H_6bmt) ligand, which has been used by us to prepare 1D and 3D LnOFs with interesting catalytic and photoluminescent properties.[15d,e] H_6tftp was self-assembled with lanthanide cations under hydrothermal conditions to produce a new family of isotypical LnOFs, formulated as $[Ln(H_3tftp)(H_2O)]$ [where $Ln^{3+} = La^{3+}$ (**1**), $(La_{0.95}Eu_{0.05})^{3+}$ (**2**), $(La_{0.95}Tb_{0.05})^{3+}$ (**3**) and $(La_{0.94}Eu_{0.03}Tb_{0.03})^{3+}$ (**4**)]. The crystal structure of **1**, isolated as large single-crystals, was ultimately unveiled by single-crystal X-ray diffraction consisting of neutral $_\infty{}^2[La(H_3tftp)(H_2O)]$ layers. To the best of our knowledge these materials constitute the first examples in which a fluorinated phosphonate organic ligand has been used for the preparation of multidimensional coordination polymers with rare-earth cations. We further note that despite the sole difference between H_6tftp and H_6bmt being the replacement of hydrogen of the aromatic ring by fluorine atoms, we could not prepare LnOF materials sharing the same crystalline structure of the previously reported 1D and 3D architectures based on residues of H_6bmt.

2. Experimental section

2.1. General instrumentation

SEM (Scanning Electron Microscopy) images were acquired using either a Hitachi S4100 field emission gun tungsten filament instrument working at 25 kV or a high-resolution Hitachi SU-70 working at 4 kV. Samples were prepared by deposition on aluminium sample holders followed by carbon coating using an Emitech K950X carbon evaporator. EDS (Energy Dispersive X-ray Spectroscopy) data and SEM mapping images were recorded using the same microscope, Hitachi SU-70, working at 15 kV and using a Bruker Quantax 400 or a Sprit 1.9 EDS microanalysis system.

Thermogravimetric analyses (TGA) were carried out using a Shimadzu TGA 50, from ambient temperature to *ca.* 800 °C, with a heating rate of 5 °C min^{-1} under a continuous stream of air at a flow rate of 20 mL min^{-1}.

Fourier Transform Infrared (FT-IR) spectra (in the range 3750–350 cm^{-1}) were recorded as KBr pellets (typically 2 mg of the sample were mixed in a mortar with *ca.* 200 mg of KBr) using a Bruker Tensor 27 spectrometer by averaging 200 scans at a maximum resolution of 2 cm^{-1}.

Elemental analyses for C and H were performed with a Truspec Micro CHNS 630-200-200 elemental analyzer at the Department of Chemistry, University of Aveiro. Analysis parameters: sample amount between 1 and 2 mg; combustion furnace temperature = 1075 °C; afterburner temperature = 850 °C. Detection method: carbon–infrared absorption, hydrogen–infrared absorption. Analysis time = 4 minutes. Gasses required: carrier – helium, combustion – oxygen, pneumatic – compressed air.

Routine Powder X-Ray Diffraction (PXRD) data for all materials were collected at ambient temperature on an X'Pert MPD Philips diffractometer (Cu $K_{\alpha 1,2}$ X-radiation, λ_1 = 1.540598 Å; λ_2 = 1.544426 Å), equipped with an X'Celerator detector and a flat-plate sample holder in a Bragg–Brentano para-focusing optics configuration (45 kV, 40 mA). Intensity data were collected by the step-counting method (step 0.04°), in continuous mode, in the *ca.* $5 \leq 2\theta \leq 50°$ range.

$^{13}C\{^1H\}$ CP MAS and ^{31}P HPDEC MAS spectra were recorded at 9.4 T on a Bruker Avance 400 wide-bore spectrometer (DSX model) on a 4 mm BL cross-polarization magic-angle spinning (CPMAS) VTN probe at 100.6 and 161.9 MHz, respectively. For the $^{13}C\{^1H\}$ CP MAS spectra the Hartmann–Hahn (HH) "sideband" matching condition $\nu_1{}^{13C} = \nu_1{}^{1H} + n\nu_R$ ($n = \pm 1$) was carefully matched by calibrating the ^1H and the ^{13}C rf field strengths; recycle delay: 3 s; contact time: 2 ms; ν_R = 15 kHz. For the ^{31}P HPDEC spectra a 90° single pulse excitation of 3.5 μs was employed; recycle delay: 60 s; ν_R = 15 kHz. Chemical shifts are quoted in parts per million (ppm) with respect to TMS for the ^{13}C nuclei, and to an 85% H_3PO_4 solution for the ^{31}P nucleus.

^1H, ^{13}C, ^{31}P and ^{19}F liquid NMR spectra were recorded with a Bruker AVANCE 300 spectrometer at 300.13, 75.47, 121.49 and 282.40 MHz, respectively. Deuterated chloroform ($CDCl_3$) or dimethylsulfoxide-d_6 (DMSO-d_6) were used as solvents. Tetramethylsilane, H_3PO_4 (85%) or hexafluorobenzene were used as internal references. Chemical shifts (δ) are quoted in ppm and the coupling constants (J) in Hz.

Mass spectra were collected using a Micromass Q-TOF2 equipment. Dichloromethane and water were used as solvent for hexaethyl((2,4,6-trifluorobenzene-1,3,5-triyl)tris(methylene)) tris(phosphonate) (L^2) and ((2,4,6-trifluorobenzene-1,3,5-triyl) tris(methylene))triphosphonic acid (H_6tftp), respectively. The employed concentration was 1 mg mL^{-1}. Samples were diluted in methanol to a concentration of 2 μL (sample) per 200 μL (methanol).

2.2. Reagents and solvents

Chemicals were readily available from commercial sources and were used as received without further purification: 1,3,5-trifluorobenzene ($C_6H_3F_3$, 98%, Alfa Aesar); chloromethyl methyl ether (C_2H_5ClO, technical grade, Sigma-Aldrich); aluminium chloride ($AlCl_3$, >98%, Merck); sodium hydrogen carbonate ($NaHCO_3$, 99%, Panreac); triethyl phosphite [$(C_2H_5O)_3P$, 98%, Sigma-Aldrich]; hydrochloric acid (HCl, 37%, Panreac); dichloromethane (CH_2Cl_2, pure, Sigma-Aldrich); methanol (CH_3OH, >99.8%, Fluka); dimethyl sulfoxide-d_6 (DMSO-d_6, 99.99%, Euriso-top); deuterated chloroform ($CDCl_3$, 99.99%, Euriso-top); potassium bromide (KBr, for infrared spectroscopy, BDH).

2.3. Synthesis of ((2,4,6-trifluorobenzene-1,3,5-triyl)tris(methylene))-triphosphonic acid (H_6tftp)

To a mixture of 1,3,5-trifluorobenzene (0.60 g, 4.54 mmol) and chloromethyl methyl ether (6.58 g, 81.7 mmol, 18 eq.), anhydrous $AlCl_3$ (10.90 g, 81.7 mmol, 18 eq.) was slowly added for about 10 min, under a nitrogen atmosphere and at 0 °C. This step was accompanied with the formation of an orange precipitate. The mixture was stirred at 0 °C for 10 min and then at 40 °C for approximately 7 h. The final dark brown solution was poured onto ice and stirred overnight. A liquid–liquid extraction was performed using dichloromethane. The organic phase was then neutralized with a saturated solution of $NaHCO_3$ and dried over anhydrous $NaSO_4$. Dichloromethane was distilled under reduced pressure and the final oily residue was purified by flash column chromatography using petroleum ether/dichloromethane (4 : 1) as eluent. The target compound, 1,3,5-tris(chloromethyl)-2,4,6-trifluorobenzene (**L^1**), was obtained as a microcrystalline white powder in 71% yield (0.90 g).

A mixture of **L^1** (0.94 g, 3.40 mmol) and triethyl phosphite (15 mL) was refluxed under a nitrogen atmosphere for approximately 3 h. After cooling to ambient temperature, the excess of triethyl phosphite was distilled under reduced pressure (**Caution!** triethyl phosphite has an extremely unpleasant smell and it is harmful; it should, therefore, always be handled inside a fume hood). The resulting oily residue was dissolved in dichloromethane and the desired compound, hexaethyl((2,4,6-trifluorobenzene-1,3,5-triyl)tris (methylene))tris(phosphonate) (**L^2**), was purified by flash column chromatography using a mixture of dichloromethane/methanol (95% : 5%) as eluent. **L^2** was isolated as a microcrystalline white powder in 75% yield (1.49 g).

To **L^2** (1.70 g, 2.92 mmol) an aqueous solution of HCl (110 mL, 6 M) was added, and the resulting reaction mixture was refluxed for approximately 20 h under continuous magnetic stirring. The reaction product was washed with dichloromethane and the aqueous phase was distilled under reduced pressure. The desired compound, ((2,4,6-trifluorobenzene-1,3,5-triyl)tris(methylene))triphosphonic acid (H_6tftp), was recovered as a microcrystalline white crystalline powder (98% yield, 1.18 g) by vacuum filtration and washed with excess acetone.

L^1: ^{1}H NMR (300.13 MHz, $CDCl_3$) δ (in ppm): 4.64 (s, 6H, CH_2).

^{13}C NMR (75.47 MHz, $CDCl_3$) δ (in ppm): 31.8–31.9 (CH_2), 111.0–111.5 (Ar–C) and 159.5 (dt, $J(^{13}C–^{19}F)$ = 258.1 Hz and $^3J(^{13}C–^{19}F)$ = 10.4 Hz, Ar–CF).

^{19}F NMR (282.40 MHz, $CDCl_3$) δ (in ppm): −138.1 (s, 3F, ArF).

L^2: ^{1}H NMR (300.13 MHz, $CDCl_3$) δ (in ppm): 1.29 (t, 18H, $J(^1H–^1H)$ = 7.07 Hz, CH_3), 3.19 (d, 6H, $J(^1H–^{31}P)$ = 21.4 Hz, $CH_2PO_3Et_2$), 4.09 (dq, 12H, $J(^1H–^1H)$ = 7.07 Hz and $J(^1H–^{31}P)$ = 7.3 Hz, CH_2CH_3).

^{13}C NMR (75.47 MHz, $CDCl_3$) δ (in ppm): 16.3–16.4 (CH_3), 21.0 (d, $J(^{13}C–^{31}P)$ = 143.2 Hz, CH_2), 62.3–62.4 (CH_2CH_3), 104.7–105.3 (Ar–C), 156.3, 156.4 and 159.7 (Ar–CF).

^{19}F NMR (282.40 MHz, $CDCl_3$) δ (in ppm): −138.7 (q, $J(^{19}F–^{31}P)$ = 5.6 Hz, 3F, ArF).

MS (TOF MS ES$^+$) m/z: 583.2 $[M+H]^+$ and 605.2 $[M+Na]^+$.

H_6tftp: ^{1}H NMR (300.13 MHz, DMSO-d_6) δ (in ppm): 2.93 (d, 6H, $J(^1H–^{31}P)$ = 20.9 Hz, CH_2).

^{13}C NMR (75.47 MHz, DMSO-d_6) δ (in ppm): 23.0 (d, $J(^{13}C–^{31}P)$ = 135.7 Hz, CH_2), 105.8–106.2 (Ar–C) and 155.5–155.8 and 158.9–159.1 (Ar–CF).

^{19}F NMR (282.40 MHz, DMSO-d_6) δ (in ppm): −139.5 (q, $J(^{19}F–^{31}P)$ = 5.6 Hz, 3F, ArF).

^{31}P NMR (121.49 MHz, DMSO-d_6) δ (in ppm): 19.4 (t, $J(^{31}P–^1H)$ = 20.4 Hz, PO_3H_2).

MS (TOF MS ES$^-$) m/z: 197.4 $[M–2H–F]^{2-}$, 413.1 $[M–H]^-$ and 451.0 $[M–2H+K]^-$.

2.4. Hydrothermal synthesis: isotypical [Ln(H_3tftp)(H_2O)] materials

A reactive mixture composed of 0.1374 g of $LaCl_3{\cdot}7H_2O$ and 0.0766 g of ((2,4,6-trifluorobenzene-1,3,5-triyl)tris(methylene))-triphosphonic acid (H_6tftp) in distilled water (*ca.* 6 mL), with an overall molar ratio of approximately 1 : 2 : 1800 (H_6tftp : La^{3+} : H_2O), was prepared. The mixture was kept under constant magnetic stirring for approximately 30 min at ambient temperature. The resulting homogeneous suspension was transferred to a Teflon-lined Parr Instrument autoclave and then placed inside a MMM Venticell oven where it remained at 180 °C for 72 h. The resulting [La(H_3tftp)(H_2O)] (**1**) material was recovered by vacuum filtration as white crystalline powder, being then washed with copious amounts of distilled water and then air-dried at ambient temperature.

The isotypical materials with 5% of Eu^{3+} (**2**) and Tb^{3+} (**3**), and the mixed-lanthanide compound with 3% of Eu^{3+} and Tb^{3+} (**4**) were prepared as described above for compound **1** while adjusting the amounts of the lanthanide chloride salts in the initial reactive mixture to the desired percentages.

Elemental CH composition (%).

Calcd for **1**: C 19.02; H 1.96. Found: C 19.00; H 1.84.

Calcd (%) for **2**: C 18.99; H 1.95. Found: C 18.99; H 1.86.

Calcd (%) for **3**: C 18.99; H 1.95. Found: C 18.86; H 1.86.

Selected FT-IR data (in cm^{-1}; from KBr pellets).

1: $\nu(H_2O)_{coord}$ = 3493*w* and 3446*w*; ν(POH) = 3213*m*; ν(–CH_2–) = 2941*w*; $\delta(H_2O)$ + ν(–C=C–) = 1673*w*, 1625*s* and 1602*m*; ν(–C=C–) = 1470*vs*; δ(P–CH_2) = 1420*m* and 1409*m*; ν(P=O) and ν(C–F) = 1350–1050*m*-*vs*; ν(P–O) = 1040–900*vs*; ν(P–C) = 763*m* and 745*m*.

2: $\nu(H_2O)_{coord}$ = 3491*w* and 3446*w*; ν(POH) = 3214*m*; ν(–CH_2–) = 2941*w*; $\delta(H_2O)$ + ν(–C═C–) = 1674*w*, 1625*s* and 1602*m*; ν(–C═C–) = 1470*vs*; δ(P–CH_2) = 1420*m* and 1410*m*; ν(P═O) and ν(C–F) = 1350–1050*m-vs*; ν(P–O) = 1040–900*vs*; ν(P–C) = 763*m* and 745*m*.

3: $\nu(H_2O)_{coord}$ = 3489*w* and 3445*w*; ν(POH) = 3216*m*; ν(–CH_2–) = 2942*w*; $\delta(H_2O)$ + ν(–C═C–) = 1660*w*, 1625*s* and 1602*m*; ν(–C═C–) = 1470*vs*; δ(P–CH_2) = 1420*m* and 1408*m*; ν(P═O) and ν(C–F) = 1350–1050*m-vs*; ν(P–O) = 1040–900*vs*; ν(P–C) = 763*m* and 745*m*.

2.5. Single-crystal X-ray diffraction studies

Single crystals of [La(H_3tftp)(H_2O)] (**1**) [where H_6tftp = ((2,4,6-trifluorobenzene-1,3,5-triyl)tris-(methylene))triphosphonic acid] were manually harvested from the reaction vessel and immediately immersed in highly viscous FOMBLIN Y perfluoropolyether vacuum oil (LVAC 140/13, Sigma-Aldrich) to avoid degradation caused by the evaporation of the solvent. Crystals were mounted on Hampton Research CryoLoops with the help of a Stemi 2000 stereomicroscope equipped with Carl Zeiss lenses.[17] The selection of a suitable single-crystal for analysis was a challenging task because they frequently presented cracks. Because of this, several data sets were collected, and the crystal model herein presented corresponds to the best solution that could be found. Data were collected on a Bruker X8 Kappa APEX II CCD area-detector diffractometer (Mo Kα graphite-monochromated radiation, λ = 0.71073 Å) controlled by the APEX2 software package[18] and equipped with an Oxford Cryosystems Series 700 cryostream monitored remotely using the software interface Cryopad.[19] Images were processed using the software package SAINT+,[20] and data were corrected for absorption by the multiscan semi-empirical method implemented in SADABS.[21] The structure was solved using the Patterson synthesis algorithm implemented in SHELXS-97,[22] which allowed the immediate location of the two crystallographically independent La^{3+} centres and most of the heaviest atoms belonging to the organic linkers. The remaining non-hydrogen atoms were located from difference Fourier maps calculated from successive full-matrix least-squares refinement cycles on F^2 using SHELXL-97.[22a,23] All the non-hydrogen atoms were successfully refined by assuming anisotropic displacement parameters.

Hydrogen atoms bound to benzylic carbon atoms and belonging to the PO–H moieties were placed at their idealized positions around the parent atoms using appropriate HFIX 23 (–CH_2–) and HFIX 147 (O–H) instructions in SHELXL. Hydrogen atoms associated with the coordinated water molecules were directly located from difference Fourier maps and included in the final structural model with the O–H and H···H distances restrained to 0.95(1) and 1.55(1) Å, respectively, in order to ensure a chemically reasonable geometry for these moieties. All hydrogen atoms were included in subsequent refinement cycles in riding motion approximation with isotropic thermal displacements parameters (U_{iso}) fixed at 1.2 × U_{eq} (for –CH_2) or 1.5 × U_{eq} (for –OH and H_2O) of the parent atoms.

The refined structure comprises a highly superimposable pair of [La(H_3tftp)] moieties in the asymmetric unit (see, for example, Fig. 3). This feature could be an indication that either the space group or the unit cell parameters could have not been properly determined. The search for other unit cell parameters and space groups did not, however, produced solutions with good merit figures. The best alternative to the adopted unit cell was a monoclinic *P*2/*m* cell with parameters of *a* = 9.47 Å, *b* = 15.06 Å, *c* = 44.45 Å and β = 93.15°. Because only 55% of the data were collected for this unit cell, and the R_{int} had the value of about 41%, the structure could not be solved.

The last difference Fourier map synthesis showed for **1** the highest peak (2.163 e Å^{-3}) and deepest hole (−1.807 e Å^{-3}) located in the neighbouring metal centres at 1.23 Å and 1.89 Å from O1W and O12, respectively. Details of the crystal data and structure refinement parameters for compound **1** are summarized in Table 1. Crystallographic details and structural drawing for the novel organic molecules reported in this paper (*i.e.*, the new tripodal organic ligand **H_6tftp** and the two intermediate molecules) are provided in the ESI.† Structural diagrams were prepared using the Diamond Version 3.2 software,[24] except for the superimposition diagram

Table 1 Crystal data collection and refinement details for [La(H_3tftp)(H_2O)] (**1**)

Formula	$C_{18}H_{22}F_6La_2O_{20}P_6$
Formula weight	1136.00
Temperature/K	150(2)
Crystal system	Triclinic
Space group	$P\bar{1}$
a/Å	9.4435(4)
b/Å	11.7657(5)
c/Å	14.9918(7)
α/°	110.335(2)
β/°	90.018(2)
γ/°	93.142(2)
Volume/Å^3	1559.23(12)
Z	2
D_c/g cm^{-3}	2.420
μ(Mo-Kα)/mm^{-1}	3.135
Crystal size/mm^3	0.04 × 0.04 × 0.01
Crystal type	Colourless plate
θ range (°)	3.54 to 25.35
Index ranges	$-11 \le h \le 11$ $-14 \le k \le 14$ $-18 \le l \le 17$
Reflections collected	44 212
Independent reflections	5677 [R_{int} = 0.0789]
Completeness to θ = 25.35°	99.2%
Final *R* indices [$I > 2\sigma(I)$][a b]	R_1 = 0.0512 wR_2 = 0.1148
Final *R* indices (all data)[a b]	R_1 = 0.0805 wR_2 = 0.1266
Weighting scheme[c]	*m* = 0.0493 *n* = 18.4769
Largest diff. peak and hole	2.163 and −1.807 e Å^{-3}
CCDC no.	952452

[a] $R_1 = \sum ||F_o| - |F_c|| / \sum |F_o|$.

[b] $wR_2 = \sqrt{\sum \left[w\left(F_o^2 - F_c^2\right)^2 \right] / \sum \left[w\left(F_o^2\right)^2 \right]}$.

[c] $w = 1/[\sigma^2(F_o^2) + (mP)^2 + nP]$ where $P = (F_o^2 + 2F_c^2)/3$.

(Fig. 3) which was prepared using Mercury CSD 3.1 Development (Build RD5).[25]

2.6. Variable-temperature powder X-ray diffraction

Variable-temperature powder X-ray diffraction data for [La(H_3tftp)(H_2O)] (**1**) were collected on a D8 Advance Bruker diffractometer (Cu $K_{\alpha1,2}$ X-radiation, λ_1 = 1.540598 Å; λ_2 = 1.544426 Å) under an air atmosphere, equipped with a LynxEye detector, curved graphite-monochromated radiation, a flat-plate low background Si wafer (911 oriented) as sample holder in a Bragg–Brentano para-focusing optics configuration (40 kV, 50 mA), and a high-temperature Anton Parr HTK1200 chamber. Intensity data were collected in the step mode (0.02°) in the range *ca.* $5 \leq 2\theta \leq 50°$. Data were collected between ambient temperature and 700 °C.

2.7. Photoluminescence

Emission and excitation spectra were recorded at 14 K and ambient temperature (298 K) using a Fluorolog-2® Horiba Scientific (Model FL3-2T) spectroscope, with a modular double grating excitation spectrometer (fitted with a 1200 grooves mm^{-1} grating blazed at 330 nm) and a TRIAX 320 single emission monochromator (fitted with a 1200 grooves mm^{-1} grating blazed at 500 nm, reciprocal linear density of 2.6 nm mm^{-1}), coupled to a R928 Hamamatsu photomultiplier, using the front face acquisition mode. The excitation source was a 450 W Xe arc lamp. Emission spectra were corrected for detection and optical spectral response of the spectrofluorimeter and the excitation spectra were corrected for the spectral distribution of the lamp intensity using a photodiode reference detector. Time-resolved measurements have been carried out using a 1934D3 phosphorimeter coupled to the Fluorolog®-3, and a Xe–Hg flash lamp (6 μs per pulse half width and 20–30 μs tail) was used as the excitation source. The low temperature measurements were performed using a helium-closed cycle cryostat with vacuum system measuring ~5×10^{-6} mbar and a Lakeshore 330 auto-tuning temperature controller with a resistance heater.

The absolute emission quantum yields were measured at ambient temperature using a quantum yield measurement system C9920-02 from Hamamatsu with a 150 W Xenon lamp coupled to a monochromator for wavelength discrimination, an integrating sphere as sample chamber and a multichannel analyzer for signal detection. Three measurements were made for each sample so that the average value is reported. The method is accurate to within 10%.

3. Results and discussion

3.1. Synthesis of ((2,4,6-trifluorobenzene-1,3,5-triyl)tris(methylene))-triphosphonic acid (H_6tftp)

The novel organic linker ((2,4,6-trifluorobenzene-1,3,5-triyl)tris(methylene))triphosphonic acid (H_6tftp) was isolated in a three-step reaction (Scheme 1). An important intermediate compound, 1,3,5-tris(chloromethyl)-2,4,6-trifluorobenzene, $\mathbf{L^1}$, was prepared (71% yield) from a chloromethylation reaction using 1,3,5-trifluorobenzene and chloromethyl methyl ether in the presence of anhydrous $AlCl_3$ for approximately 7 h. To isolate $\mathbf{L^2}$ a Michaelis–Arbuzov reaction was employed by refluxing a mixture of $\mathbf{L^1}$ and triethyl phosphite for approximately 3 h. The excess of triethyl phosphite was distilled under reduced pressure and $\mathbf{L^2}$, [hexaethyl((2,4,6-trifluorobenzene-1,3,5-triyl)-tris(methylene))tris(phosphonate)], was isolated as a white powder in 75% yield after being purified by flash column chromatography.

The last step consisted of an acid hydrolysis where an aqueous solution of HCl (6 M) was added to $\mathbf{L^2}$ and the reaction mixture refluxed for 20 h. The target compound H_6tftp was isolated as a white crystalline powder in quantitative yields (*ca.* 98%). H_6tftp and its intermediate molecules $\mathbf{L^1}$ and $\mathbf{L^2}$ were fully characterized by NMR spectroscopy and mass spectrometry. Their crystal structures were further unveiled by single-crystal X-ray diffraction (see Experimental Section and Fig. S1 to S15 in the ESI for further details†).

3.2. Hydrothermal synthesis of isotypical [Ln(H_3tftp)(H_2O] materials

The self-assembly between the new tripodal organic ligand ((2,4,6-trifluorobenzene-1,3,5-triyl)-tris(methylene))triphosphonic acid (H_6tftp) and lanthanide(III) chloride hydrates, under hydrothermal conditions (180 °C for 72 h), afforded a new family of MOF structures composed of three isotypical materials formulated as [Ln(H_3tftp)(H_2O)] [where Ln^{3+} = La^{3+} (**1**), $(La_{0.95}Eu_{0.05})^{3+}$ (**2**) and $(La_{0.95}Tb_{0.05})^{3+}$ (**3**)]. Compound **1** was the only one that could be isolated with suitable particle size to be investigated by single-crystal X-ray diffraction. Phase identification of the mixed-lanthanide materials **2** and **3** as microcrystalline powders was performed instead using powder X-ray diffraction. Elemental analysis, electron microscopy (Fig. S16 and S17 in the ESI†), solid-state NMR (Fig. 7 and S21 in the ESI†) and FT-IR spectroscopy (Fig. S22 in the ESI†) were also used in tandem to evaluate phase purity and homogeneity of the bulk materials.

Fig. 1 shows the powder X-ray diffraction patterns (PXRD) and Scanning Electron Microscopy (SEM) images of all materials. PXRD patterns indicate that compounds are crystalline and share the same crystalline phase. Concerning morphology it is clear that all compounds have the same crystal habit showing the presence of block-like crystals. A notable feature stands, nevertheless, out: compound **1** possesses crystalline block-like particles with sizes in the tens of micrometers; the inclusion of 5% of Eu^{3+} or Tb^{3+} leads to a reduction of the average particle size of **2** and **3**, with this feature being significantly more evident in the latter material.

3.3. Crystal structure of [La(H_3tftp)(H_2O)]

The crystal structure of [La(H_3tftp)(H_2O)] (**1**) was unveiled from single-crystal X-ray diffraction studies (Table 1). Compound **1** crystallizes in the centrosymmetric triclinic $P\bar{1}$ space group, with the asymmetric unit (asu) being composed of two La^{3+} metal centers, two whole residues of

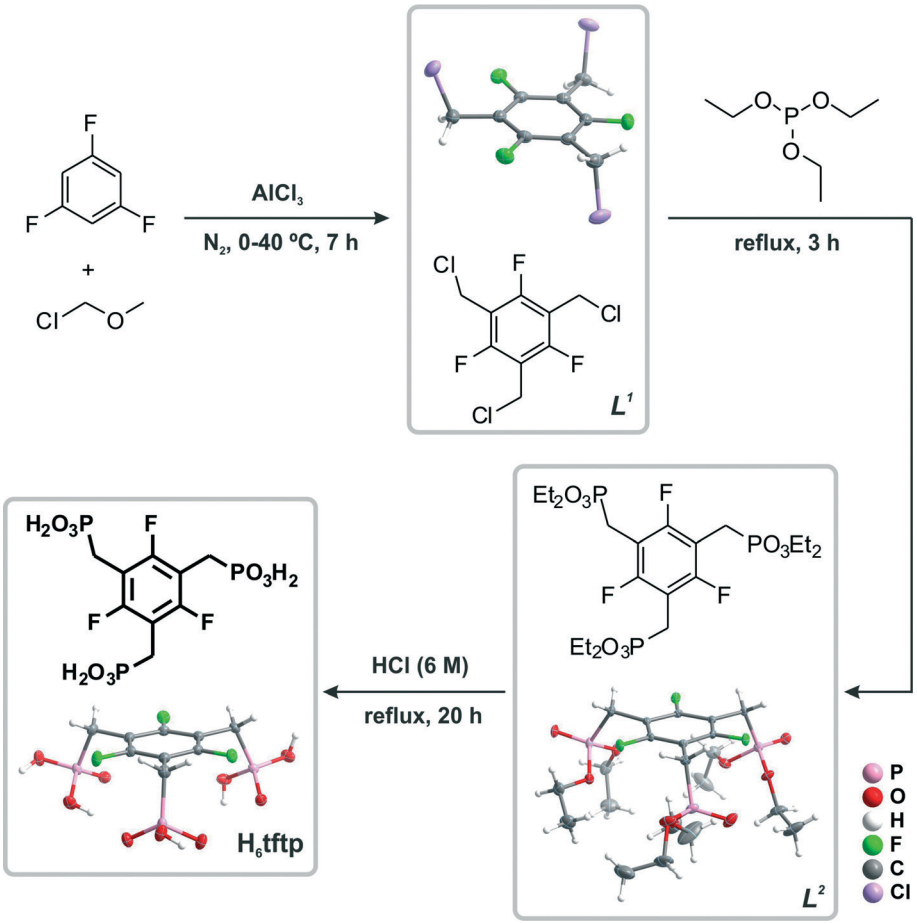

Scheme 1 Synthetic route for the preparation of ((2,4,6-trifluorobenzene-1,3,5-triyl)tris(methylene))triphosphonic acid (H_6tftp). The crystal structures of H_6tftp and of the synthetic intermediates (L^1 and L^2) are also represented (see Fig. S13 to S15 and Table S1 in the ESI for additional crystallographic details; non-hydrogen atoms are represented as thermal ellipsoids†).

((2,4,6-trifluorobenzene-1,3,5-triyl)tris(methylene))triphosphonic acid $(H_3tftp)^{3-}$ residues and two coordinated water molecules (see Fig. S18 in the ESI for a representation of the asu†).

The two crystallographically independent La^{3+} metal centers are heptacoordinated, $\{LaO_7\}$, to one water molecule and six independent phosphonate groups from four H_3tftp^{3-} residues. All phosphonate groups bear an uncoordinated –OH moiety with the two other oxygen atoms being connected to La^{3+} metal centers in a typical μ_2-*O*,*O*′ bridging mode. The La–O bond lengths to phosphonate groups range from 2.361(6) to 2.595(7) Å and the La–O_{water} distances are 2.591(6) and 2.593(6) Å. The O–La–O angles comprising the coordination spheres were found in the 73.3(2)–161.5(2)° range (see Fig. 2 and Table 2 for additional geometrical details). The overall coordination environment of the metal centers resembles, thus, a monocapped trigonal prism, with the trigonal and quadrangular internal angles in the ranges 43.4(2)–91.7(3)° and 76.7(2)–100.6(2)°, respectively (Fig. 2).

As shown in Fig. 3 the crystallographically independent pairs of metal centers and organic residues are highly superimposable. Moreover, the calculated root mean squares (rms) of 0.005 and 0.04 Å for the coordination spheres of the lanthanum atoms and the organic residues, respectively, are comparable with the experimental error of the atomic positions (for instance, the average C–C bond precision is 0.0133 Å). This fact could, in principle, indicate problems in the determination of cell parameters and/or the space group of compound **1**. Nevertheless, our attempts to find better cell parameters or space groups, always gave the crystallographic data displayed in Table 1 as the best choice. Additionally, the finding of six ^{31}P resonances in the solid-state NMR spectrum of **1**, and the existence of nine Stark components in the $^5D_0 \rightarrow {}^7F_2$ transition at 14 K (see dedicated sections for further details) for the isotypical compound **2**, agree well with our proposal for the structural model.

The combination of the H_3tftp^{3-} organic residues and La^{3+} metal centers forms a two-dimensional $_\infty{}^2[La(H_3tftp)(H_2O)]$ neutral coordination polymer placed on the *ac* lattice plane of the unit cell (Fig. 4). Despite the hydrophobic aromatic rings of H_3tftp^{3-} being located in the walls of the polymeric layers, they are not engaged in π–π stacking interactions. Weak supramolecular F···F interactions are present within the hydrophobic wall (see legend of Fig. 4 for additional details), with all the C–F···F angles being in the 139.6(6)–142.0(6)° range. The similarity between these values and their interaction angles allows us to classify unequivocally these

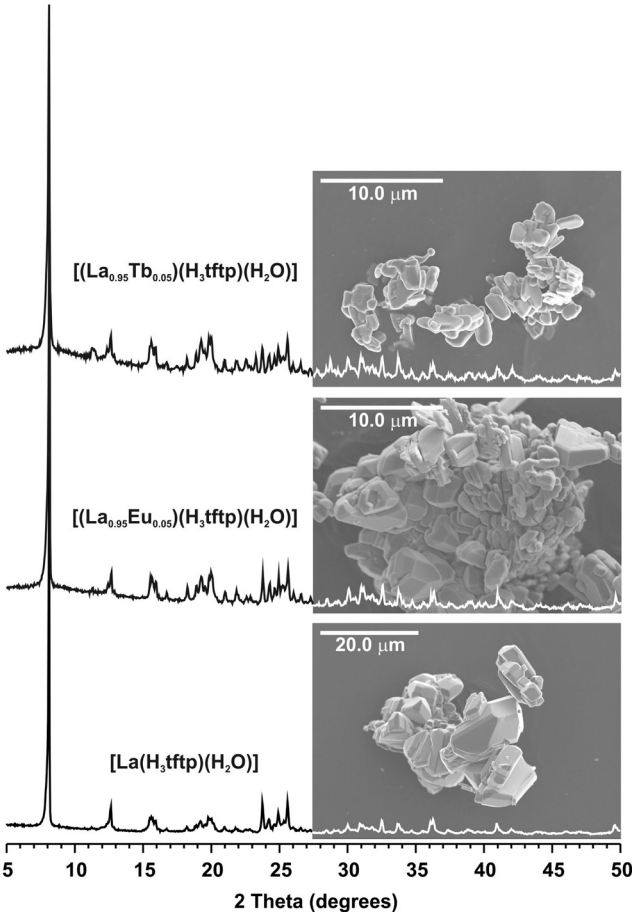

Fig. 1 Powder X-ray diffraction patterns and SEM images of [Ln(H$_3$tftp)(H$_2$O)] materials [where Ln^{3+} = La^{3+} (**1**), $(La_{0.95}Eu_{0.05})^{3+}$ (**2**) and $(La_{0.95}Tb_{0.05})^{3+}$ (**3**)] prepared (under hydrothermal conditions) at 180 °C for 72 h.

Table 2 Bond lengths (in Å) and angles (in degrees) for the two crystallograpically independent La^{3+} coordination environments present in [La(H$_3$tftp)(H$_2$O)] (**1**)[a]

La1–O14	2.361(6)	La2–O9^{iii}	2.374(6)
La1–O8	2.370(6)	La2–O13	2.371(6)
La1–O16^{i}	2.443(6)	La2–O1^{iv}	2.444(6)
La1–O6	2.458(6)	La2–O12	2.465(6)
La1–O10^{ii}	2.499(6)	La2–O4	2.505(6)
La1–O18^{ii}	2.595(7)	La2–O3	2.575(7)
La1–O1W	2.593(6)	La2–O2W	2.591(6)
O14–La1–O8	122.8(2)	O13–La2–O9^{iii}	122.4(2)
O14–La1–O16^{i}	139.4(2)	O13–La2–O1^{iv}	86.3(2)
O8–La1–O16^{i}	85.7(2)	O9^{iii}–La2–O1^{iv}	139.3(2)
O14–La1–O6	75.7(2)	O13–La2–O12	74.7(2)
O8–La1–O6	74.7(2)	O9^{iii}–La2–O12	76.1(2)
O16^{i}–La1–O6	86.7(2)	O1^{iv}–La2–O12	86.3(2)
O14–La1–O10^{ii}	75.3(2)	O13–La2–O4	73.3(2)
O8–La1–O10^{ii}	74.1(2)	O9^{iii}–La2–O4	75.3(2)
O16^{i}–La1–O10^{ii}	144.7(2)	O1^{iv}–La2–O4	144.8(2)
O6–La1–O10^{ii}	114.4(2)	O12–La2–O4	114.3(2)
O14–La1–O1W	128.4(2)	O13–La2–O3	161.5(2)
O8–La1–O1W	88.8(2)	O9^{iii}–La2–O3	75.8(2)
O16^{i}–La1–O1W	74.4(2)	O1^{iv}–La2–O3	79.8(2)
O6–La1–O1W	155.9(2)	O12–La2–O3	116.1(2)
O10^{ii}–La1–O1W	76.4(2)	O4–La2–O3	112.1(2)
O14–La1–O18^{ii}	75.5(2)	O13–La2–O2W	88.4(2)
O8–La1–O18^{ii}	161.4(2)	O9^{iii}–La2–O2W	128.3(2)
O16^{i}–La1–O18^{ii}	80.6(2)	O1^{iv}–La2–O2W	74.9(2)
O6–La1–O18^{ii}	116.8(2)	O12–La2–O2W	155.5(2)
O10^{ii}–La1–O18^{ii}	110.7(2)	O4–La2–O2W	76.1(2)
O1W–La1–O18^{ii}	75.4(2)	O3–La2–O2W	76.3(2)

[a] Symmetry transformations used to generate equivalent atoms: (i) $-x, 2-y, 2-z$; (ii) $-1+x, y, z$; (iii) $1+x, y, z$; (iv) $-x, 2-y, 1-z$.

interactions as type I, considering them thus as weak in nature. Indeed, for the F···F interactions being considered strong (type II), the C–F···F angles should be markedly distinct with values of approximately 90 and 180°.[26] Instead, the fluorine atoms are engaged in intramolecular C–H···F interactions (not shown).

All phosphonate groups point to the interlamellar space forming a lanthanum oxide layer and an intricate hydrogen bond network as depicted in Fig. 5. All oxygen atoms of this network are located within a layer with thickness of *ca.* 1.8 Å, also parallel to the *ac* lattice plane. Two pairs of rings with graph set motifs $R^2_2(6)$ and $R^2_2(8)$ are the most remarkable features of this network. The $R^2_2(8)$ set motifs are formed by two hydrogenphosphonate groups (with O···O distances ranging from 2.568(9) to 2.692(9) Å and O–H···O interaction angles between *ca.* 153 and 161°). The $R^2_2(6)$ graph set motifs comprise one hydrogenphosphonate group and one water molecule (with internuclear O···O distances ranging from 3.109(8) to 3.154(9) Å and O–H···O interaction angles between 113 and 143°; for further geometrical details see Table 3). Ultimately, the most significant packing forces between layers are weak van der Waals interactions. This structural feature can ultimately be related to the low crystal robustness of

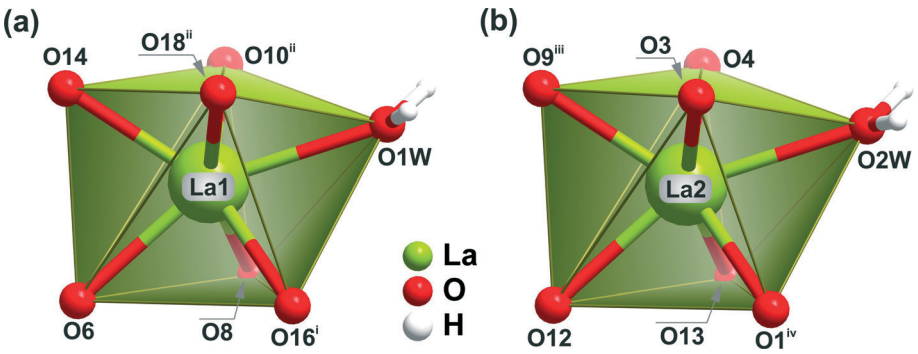

Fig. 2 Polyhedral representation of the {LaO$_7$} distorted monocapped trigonal prism coordination environments of the two crystallographic independent La^{3+} centers present in [La(H$_3$tftp)(H$_2$O)] (**1**): (a) La1 and (b) La2. For selected bond lengths and angles see Table 2.

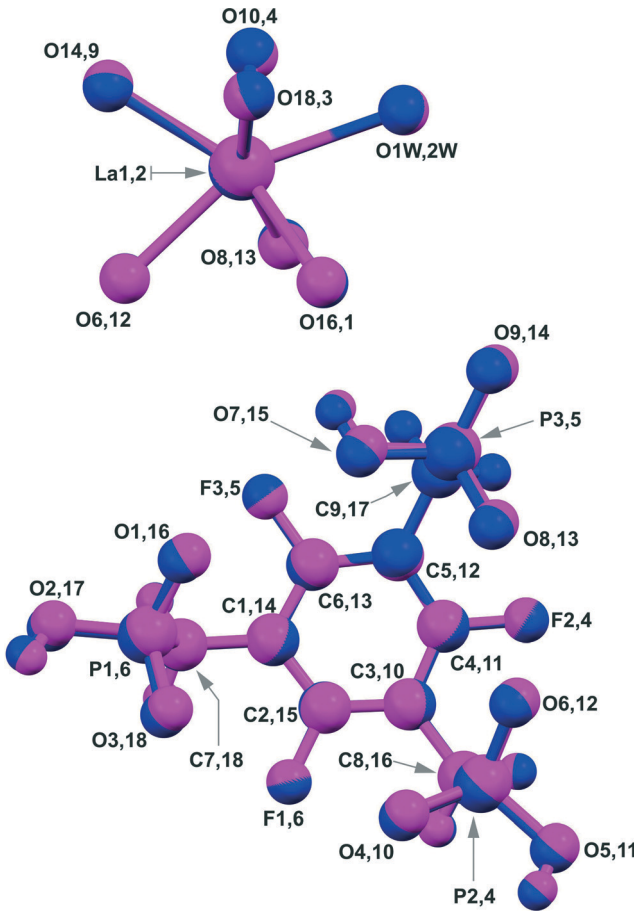

Fig. 3 Structure overlay of the (a) two coordination environments around the La^{3+} metallic centres, La1 in blue and La2 in pink, and of the (b) two crystallographic independent residues of ((2,4,6-trifluorobenzene-1,3,5-triyl)tris(methylene))triphosphonic acid (H_3tftp^{3-}). The organic ligand comprising the P1 to P3 atoms is depicted in blue and the organic ligand containing the P4 to P6 atoms is represented in pink. The first and second numbers appearing in the atom labels correspond to the blue and pink entities, respectively. Symmetry transformations used to generate equivalent atoms for the La^{3+} coordination spheres were omitted for clarity. The geometric coordinates of the atoms were adjusted using the "structure overlay" command in the software package Mercury CSD 3.1. The rms values were calculated as *ca.* 0.005 and 0.04 Å for the metal centers and organic linkers, respectively.

1 and further explains the great difficulty of finding suitable single-crystals for X-ray diffraction studies.

3.4. Topological studies

The mathematical simplification of the two-dimensional $_\infty^2$[La(H_3tftp)(H_2O)] neutral coordination polymer present in **1** into nodes and connecting rods permits the systematization of the network and a more suitable comparison with other related materials. Alexandrov *et al.*[27] suggested that any PBU in a MOF (ligand or atoms) connecting more than two moieties (μ_n) should ultimately be considered as a network node. In this fashion, in compound **1** all crystallographically independent moieties (the two La^{3+} cations and the two organic ligands) must then be considered as network nodes.

Calculations performed with the software package TOPOS[28] revealed that compound **1**, and the remaining members of the isotypical series, can ultimately be envisaged as the typical 4-connected uninodal square layer network. Indeed, topologically the four crystallographically independent moieties share exactly the same connectivity and coordination sequences up to the 10th shell (N_{10} = 221) as depicted in Fig. 6.

3.5. Solid-state NMR and FT-IR spectroscopic studies

In order to have more insight on the composition of the asymmetric unit and phase purity of the bulk materials, solid-state NMR studies were performed in the material containing the La^{3+} diamagnetic metallic center: [La(H_3tftp)(H_2O)] (**1**). ^{31}P MAS spectrum exhibits, in the isotropic region, two well-resolved resonances. After deconvolution, six peaks centered at *ca.* 8.4, 9.6, 10.6, 11.8, 16.9 and 17.0 ppm were found (Fig. 7), agreeing well with the presence of six crystallographic distinct phosphorus sites. Peak deconvolution and integration, including the spinning sidebands, provides a ratio of *ca.* 1.00 : 1.00 : 1.00 : 1.00 : 1.00 : 1.00. In the $^{13}C\{^1H\}$ CP MAS spectrum (Fig. S21 in the ESI†) it is possible to observe three distinct spectral regions: the –CH_2– groups appear as a broad peak centered at *ca.* 23.2 ppm; the aromatic C–C and C–F moieties appear in the 100–115 ppm (peaks at *ca.* 106.0 and 108.6 ppm) and 150–170 ppm (peaks at *ca.* 156.8, 157.8, 159.3 and 160.2 ppm) spectral ranges, respectively. These data are consistent with the crystallographic studies performed, agreeing particularly well with the presence of two organic ligands in the asymmetric unit of compound **1**.

FT-IR spectroscopy studies (see Fig. S22 in the ESI†) further indicate that the bulk [Ln(**H_3tftp**)(H_2O)] materials [where Ln^{3+} = La^{3+} (**1**), $(La_{0.95}Eu_{0.05})^{3+}$ (**2**) and $(La_{0.95}Tb_{0.05})^{3+}$ (**3**)] are indeed isotypical. In this context, we shall discuss in detail some spectral features for compound **1**, all the considerations also being valid for materials **2** and **3**. The FT-IR spectrum of **1** is composed of two relevant spectral regions. In the 3750–2500 cm^{-1} range one can observe: (i) the typical ν(O–H) stretching vibrational modes of the coordinated water molecules (at *ca.* 3493 and 3446 cm^{-1}) and of the PO–H groups (at *ca.* 3213 cm^{-1}); and (ii) a weak and sharp band observed at *ca.* 2941 cm^{-1} is attributed to the ν(C–H) stretching vibration of the –CH_2– groups. Below 1800 cm^{-1} the FT-IR spectrum of **1** is complex with a large number of medium-to-very strong vibration bands.[29] At *ca.* 1673, 1625 and 1602 cm^{-1} it is possible to observe the $\delta(H_2O)$ and ν(–C=C–) in-plane deformations. The very intense peak at around *ca.* 1470 cm^{-1} is attributed again to a ν(–C=C–) stretching vibration mode of the aromatic ring, being frequently observed with the presence of electron acceptors connected to the aromatic rings. Two medium intensity bands peaking at *ca.* 1420 and 1409 cm^{-1} belong to the –CH_2– deformation vibrational modes from the P–CH_2 groups. Additionally, the ν(P=O) and ν(C–F) modes appear in the 1350–1050 cm^{-1} range, followed by a set of vibration bands between 1040 and 900 cm^{-1} attributed to the ν(P–O)

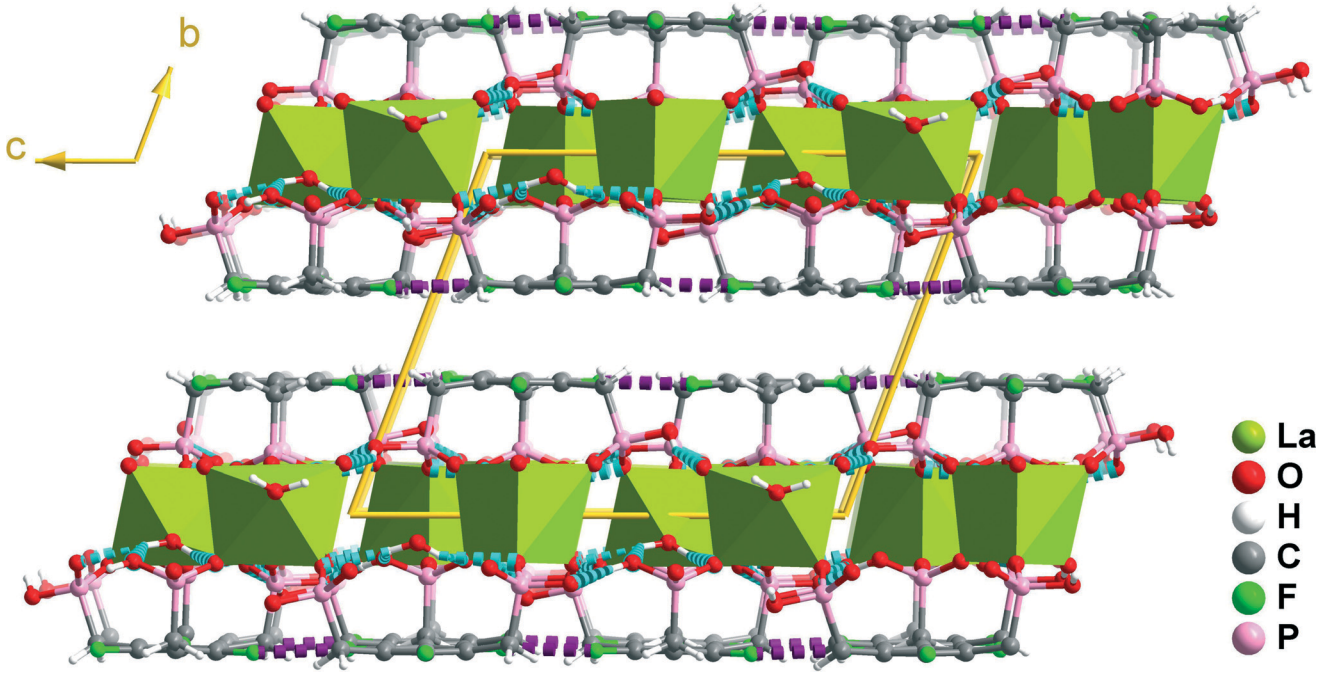

Fig. 4 Crystal packing of [La(H_3tftp)(H_2O)] (**1**) viewed in perspective along the [100] direction of the unit cell. The coordination environments around the metal centers are shown as green polyhedra. Hydrogen bonds are represented as dashed blue lines (for geometrical details about the hydrogen bonding geometry see Table 3). F···F interactions are depicted as dashed violet lines: F3···F4 2.848(9) Å and F2···F5 2.864(9) Å; interaction angles C–F3···F4–C −177.8(1)° and C–F2···F5–C −178.3(1)°; ∠(C–F···F) ranging from 139.6(6) to 142.0(6)°.

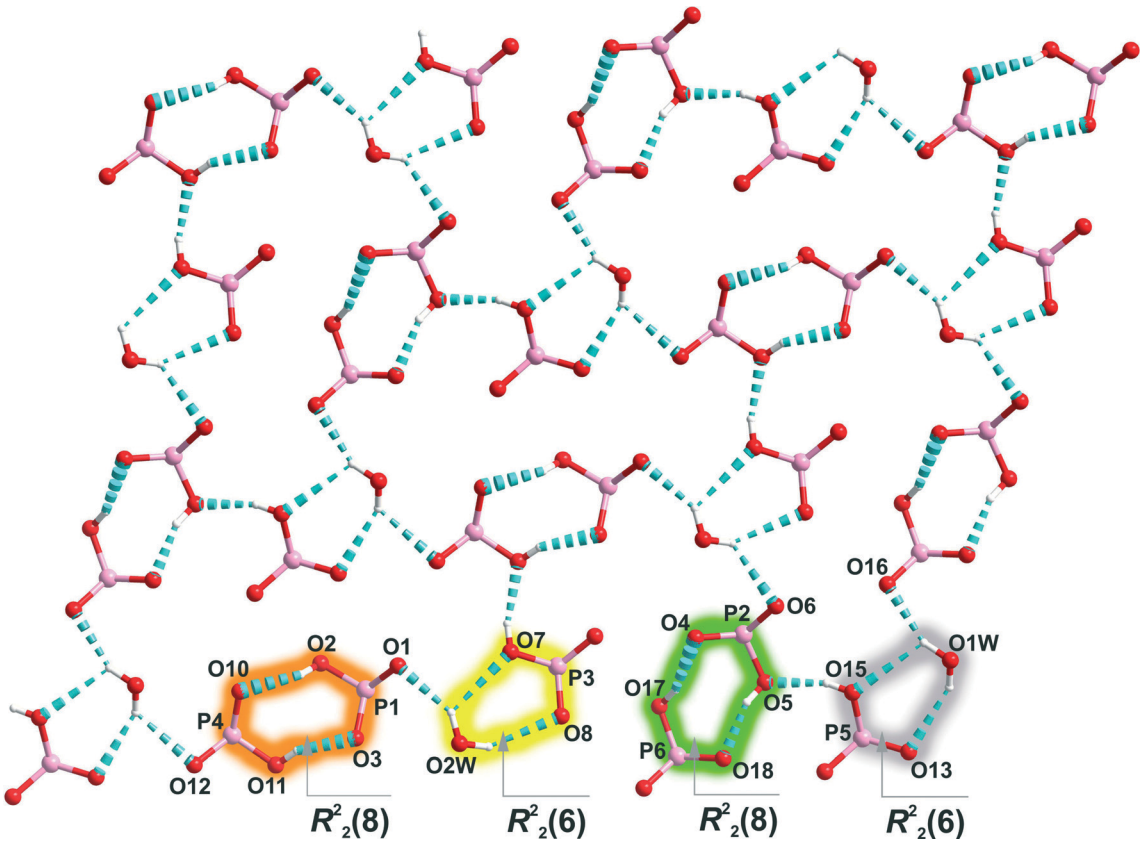

Fig. 5 Schematic representation of the hydrogen bonding network present in the crystal structure of [La(H_3tftp)(H_2O)] (**1**) emphasizing the presence of four different rings with graph set motifs of $R^2_2(6)$ (highlighted in yellow and gray) and $R^2_2(8)$ (highlighted in orange and green). Symmetry codes used to generate equivalent atoms have been omitted for clarity. For geometrical details on the represented hydrogen bonds see Table 3.

Table 3 Hydrogen bonding geometric details (distances in Å and angles in degrees) for the interactions present in [La(H_3tftp)(H_2O)] (**1**)[a]

D–H···A	*d*(D···A)	∠(DHA)
O1W–H1X···O16^{ii}	2.931(9)	155
O1W–H1X···O15^{ii}	3.114(9)	113
O1W–H1Y···O12^{ii}	3.054(10)	129
O1W–H1Y···O13^{ii}	3.132(9)	146
O2W–H2X···O1	2.960(9)	146
O2W–H2X···O7	3.109(8)	120
O2W–H2Y···O6	3.049(9)	132
O2W–H2Y···O8	3.154(9)	143
O2–H2···O10^{v}	2.682(9)	154
O5–H5···O18^{vi}	2.578(9)	152
O7–H7···O11^{iv}	2.687(9)	164
O11–H11···O3^{v}	2.568(9)	153
O15–H15···O5^{i}	2.692(9)	161
O17–H17···O4^{vi}	2.666(8)	159

[a] Symmetry transformations used to generate equivalent atoms: (i) $-x$, $2-y$, $2-z$; (ii) $-1+x$, y, z; (iv) $-x$, $2-y$, $1-z$; (v) $1-x$, $2-y$, $1-z$; (vi) $1-x$, $2-y$, $2-z$.

modes. The ν(P–C) stretching vibrations are centered at *ca.* 763 and 745 cm^{-1}.[29]

3.6. Thermogravimetry and thermodiffractometry

The thermal stability of the isotypical [Ln(**H_3tftp**)(H_2O)] materials [where Ln^{3+} = La^{3+} (**1**), $(La_{0.95}Eu_{0.05})^{3+}$ (**2**) and $(La_{0.95}Tb_{0.05})^{3+}$ (**3**)] was investigated between ambient temperature and *ca.* 800 °C. We note that the thermogravimetric curves of the three materials present slightly different profiles (see Fig. S23 in the ESI†), with this fact being attributed to the decrease of the average particle size of compounds **2** and **3** (see SEM images in Fig. 1): it is expected that materials with smaller average particle size, thus showing a higher surface area, to be less thermally stable, hence leading to distinct overall thermal stabilities. In this context, it is observed that the decomposition of **2** and **3** starts at lower temperatures than that registered for **1**. This behavior is more evident for compound **3** (corresponding to the smallest average particle size). In spite of these differences the thermal decomposition of materials **1**–**3** occurs in a rather similar fashion as shown in Fig. S21 in the ESI.† In order to understand the temperature effect in the crystal structure itself, variable-temperature powder X-ray diffraction (VTPRXD) studies on bulk **1** were performed between *ca.* 30 to 700 °C.

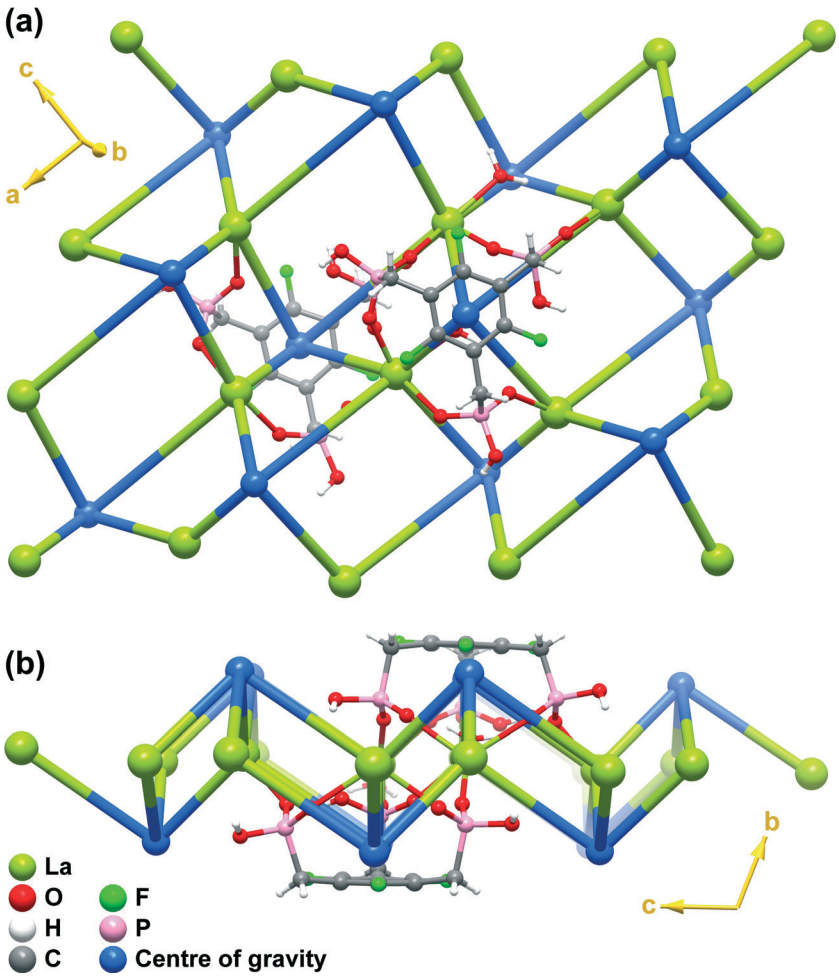

Fig. 6 Topological representation (top and side views) of the common 4-connected uninodal square layered network of [La(H_3tftp)(H_2O)] (**1**). Atoms comprising the asymmetric unit of **1** are also represented in ball-and-stick mode.

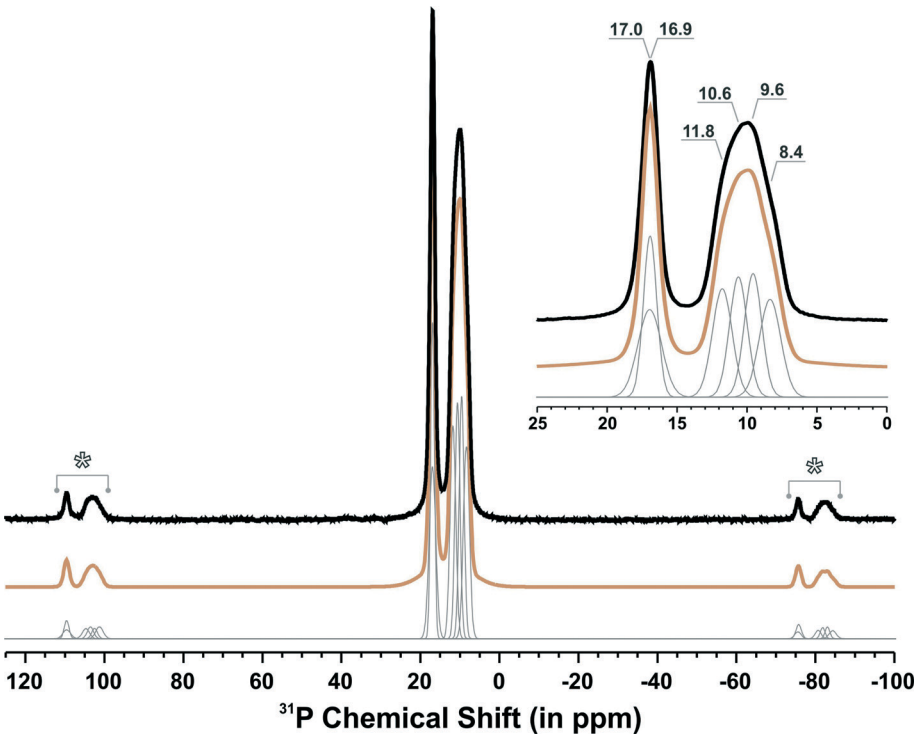

Fig. 7 Experimental (black) and deconvoluted (light brown) ^{31}P HPDEC MAS spectra of [La(**H$_3$tftp**)(H$_2$O)] (**1**). Spinning sidebands are denoted using an asterisk. Peak deconvolution and integration throughout the entire spectral range (*i.e.*, including the spinning sidebands) gives a ratio of *ca.* 1.00 : 1.00 : 1.00 : 1.00 : 1.00 : 1.00 for the isotropic resonances peaking at *ca.* 8.4, 9.6, 10.6, 11.8, 16.9 and 17.0 ppm, respectively. The gray lines represent the individual fits for the single resonances.

Compound **1** is thermally stable from ambient temperature to approximately 200 °C. In this temperature range no weight loss is observed (Fig. 8 – *bottom left*), with the crystal structure of **1** remaining intact (Fig. 8 – *top right*). The first weight loss occurs between *ca.* 207 and 357 °C, being attributed to the release of the coordinated water molecules and the beginning of the material deterioration. As observed from the VTPRXD patterns a dramatic loss of crystallinity occurs during the first weight loss. After this, several weight losses are observed, leading to the formation of an amorphous residue at approximately 450 °C. At *ca.* 700 °C a residue composed of a mixture of lanthanum catena-triphosphate (LaP_3O_9, ICDD 00-033-0717) and monazite ($LaPO_4$, ICDD 01-071-6745) was identified by powder X-ray diffraction (PDF4+ 2012 release ICDD database).

3.7. Photoluminescence

The photoluminescence properties of the isotypical mixed-lanthanide [$(La_{0.95}Eu_{0.05})$(H$_3$tftp)(H$_2$O)] (**2**), [$(La_{0.95}Tb_{0.05})$(H$_3$tftp)(H$_2$O)] (**3**) and [$(La_{0.94}Eu_{0.03}Tb_{0.01})$(H$_3$tftp)(H$_2$O)] (**4**) materials were investigated both at ambient and low temperature and compared with the starting H$_3$tftp ligand and the former [La(H$_3$tftp)(H$_2$O)] (**1**) compound. The excitation spectra of **2** and **3**, while monitoring the emission at 616 and 542 nm within the Eu^{3+} $^5D_0 \rightarrow {}^7F_2$ and Tb^{3+} $^5D_4 \rightarrow {}^7F_5$ transitions, respectively, are shown in Fig. 9. Spectra are dominated by a broad UV band (240–280 nm) which may be attributed to the π–π* transitions associated with the organic linkers. This assignment was further confirmed by monitoring the singlet UV emission at 330 nm in both the H$_6$tftp ligand and compound **1** (see Fig. 9 and Fig. S24 in the ESI†). The excitation of **1** is slightly red shifted relatively to the one of H$_6$tftp and resembles the UV broad band observed for compounds **2** and **3**. The additional sharp extra lines in the spectra of **2** and **3** were identified as the intra-4f^6 transitions $^7F_0 \rightarrow {}^5D_{1-4}$, $^5L_6$, $^5G_{2-6}$, $^5H_{3-7}$ and $^5F_{1-5}$ of Eu^{3+}, and as the intra-4f^8 transitions $^7F_6 \rightarrow {}^5D_{2-4}$ and ^5G_J of Tb^{3+}.

The emission spectra of compounds **2** and **3**, recorded at ambient temperature (using an excitation wavelength of 270 nm), are shown in Fig. 10. The sharp lines are assigned to the transitions between the first excited non-degenerate $^5D_0$ state and the $^7F_{0-4}$ levels of the fundamental Eu^{3+} septet, and between the first excited state $^5D_4$ and the $^7F_{6-0}$ levels of Tb^{3+} for **2** and **3**, respectively. The emission spectrum of **2** shows a predominance of the $^5D_0 \rightarrow {}^7F_2$ transition comparatively to the $^5D_0 \rightarrow {}^7F_1$. The identification of, at least, nine Stark components in this spectrum for the $^5D_0 \rightarrow {}^7F_2$ transition at 14 K (inset in Fig. 10) clearly indicates the presence of at least two low-symmetry Eu^{3+} environments in the crystal structure. This feature agrees well with the performed crystallographic studies (see dedicated section for further details). The ambient temperature $^5D_0$ and $^5D_4$ lifetimes of Eu^{3+}- and Tb^{3+}-based materials were determined by monitoring the emission decay curves within the maximum of the $^5D_0 \rightarrow {}^7F_2$ and $^5D_4 \rightarrow {}^7F_5$ transitions, using an excitation at 393 and 376 nm, respectively (Fig. S25 in the ESI†). Both decay curves

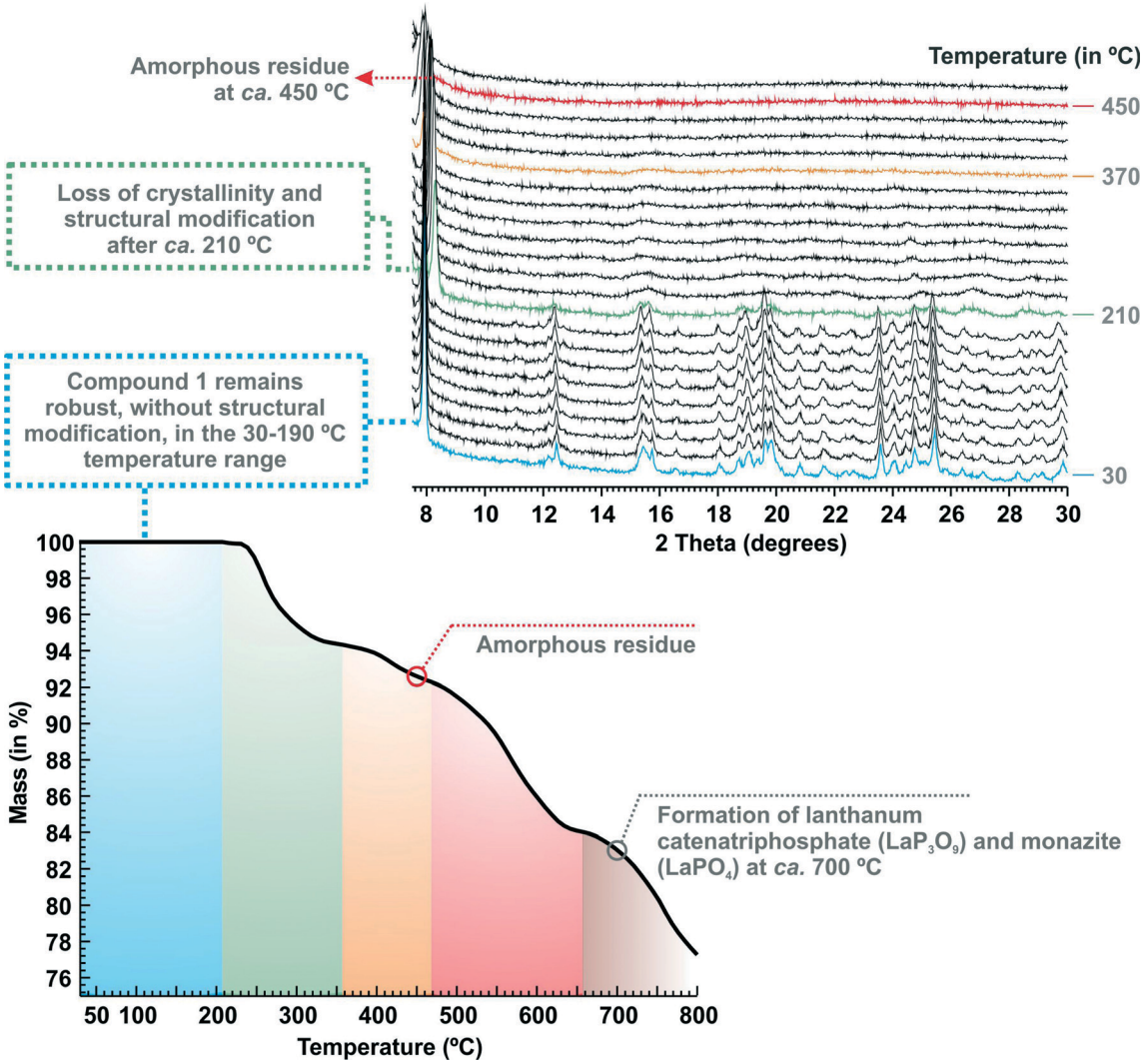

Fig. 8 Thermogram and variable-temperature powder X-ray diffraction studies for compound [La(H_3tftp)(H_2O)] (**1**).

can be fitted by single exponential functions, yielding lifetimes of 0.51 ± 0.01 and 1.26 ± 0.01 ms for **2** and **3**, respectively. For distinct excitation and/or the emission detection wavelengths we have systematically obtained identical lifetimes values. Considering the presence of the two distinct Ln^{3+} environments in the crystal structures, the determination of single exponential decay curves arises as a further indication of the strong similarity between the two crystallographically independent Ln^{3+} sites in terms of the emission decay lifetime. Note that, based on crystallographic studies, both Ln^{3+} metal centers have the same coordinated elements on the first sphere (seven oxygen atoms: six belonging to six independent phosphonate groups and one belonging to a water molecule) with very similar Ln–O distances (see Table 2 for further details). At 14 K the $^5D_0$ decay curve of **2** has also a single exponential behaviour independently of the excitation and emission wavelengths, yielding a lifetime of 0.56 ± 0.01 ms (data not shown). Noteworthy, the calculated lifetime is not dependent on the emission wavelength detection.

The measured absolute emission quantum yield, *ca.* 1% at 270 nm and 12% at 393 nm for **2**, and *ca.* 7% at 270 nm and 4% at 376 nm for **3**, are relatively low. The low emission performance of the mixed-lanthanide Ln^{3+}-based light emitters is certainly the result of the combination of two main factors: (i) the presence of one water molecule in the first coordination sphere of the crystallographically independent Ln^{3+} cations, and (ii) an inefficient ligand-to-Ln^{3+} energy transfer mechanism. The latter assumption is further supported by the observation of the singlet ligand emission of **1** in the UV spectral region: for compounds **2** and **4**, under 265 nm excitation at ambient temperature (Fig. S24 and S26 in ESI,† respectively), the short lifetime is inferior to 10 μs, which is also below the range of the phosphorimeter used. The UV emission of **1** is identical to the UV broad emission band of **2**, and slightly red-shifted relatively to the emission of H_6tftp ligand (see Fig. S24 in ESI†). The complete UV–Vis emission spectra of **4** demonstrates the relevance of this emission, relatively to the visible Eu^{3+} and Tb^{3+} emissions, particularly

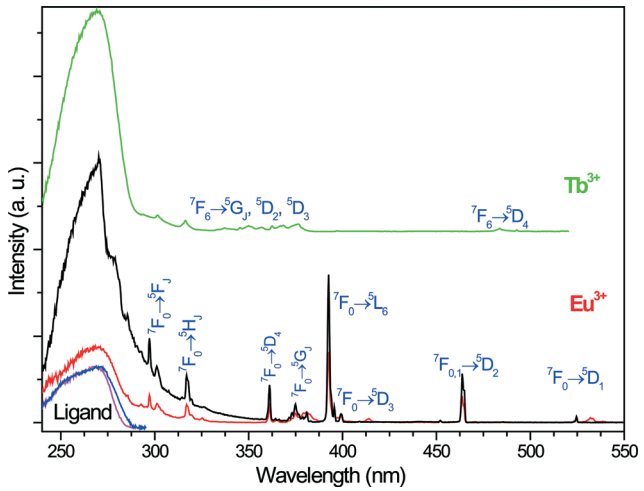

Fig. 9 Excitation spectra of $[(La_{0.95}Eu_{0.05})(H_3tftp)(H_2O)]$ (**2**) at ambient temperature (red line) and at 14 K (black line), and of $[(La_{0.95}Tb_{0.05})(H_3tftp)(H_2O)]$ (**3**) at ambient temperature (green line). Emission was monitored at 616 and 542 nm for the Eu^{3+}- and Tb^{3+}-based materials, respectively. The ambient temperature excitation spectra of the H_6tftp ligand (magenta line) and of $[La(H_3tftp)(H_2O)]$ (**1**) (blue line), while detecting the emission fluorescence at 330 nm, are provided for comparative purposes.

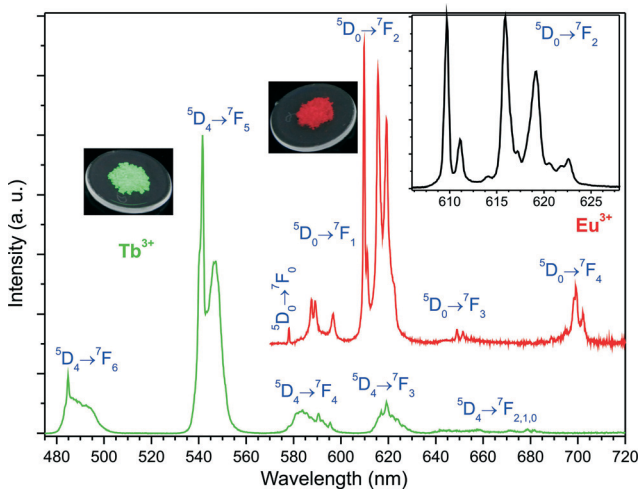

Fig. 10 Emission spectra of $[(La_{0.95}Eu_{0.05})(H_3tftp)(H_2O)]$ (**2**) (red line) and $[(La_{0.95}Tb_{0.05})(H_3tftp)(H_2O)]$ (**3**) (green line) at ambient temperature while using an excitation wavelength of 270 nm. The inset shows a magnification of the Eu^{3+} $^5D_0 \rightarrow {}^7F_2$ transition recorded at 14 K.

at ambient temperature (see Fig. S26 in ESI†): the integrated intensity represents 38% and of the sample emission at ambient temperature. At low temperature an additional background band in the entire visible region is also visible, most probably arising from the phosphorescence of the ligand. The excitation spectra of **4** (Fig. S27 in ESI†) in the Eu^{3+} (616 nm) and Tb^{3+} (542 nm) emissions are similar to those of **2** and **3**, respectively. This evidences the lack of the common Tb^{3+} to Eu^{3+} energy transfer. As a result, the relative intensities of the Eu^{3+} and Tb^{3+} emissions do not change considerably with the change in temperature (Fig. S28 in ESI†). The corresponding CIE (Commission International d'Eclairage) chromaticity (x,y) color coordinates (shown in Fig. S29 of the ESI,† together with those of **2** and **3**) evidences a small variation for the probed temperature range. In this context compound **4** is not suitable to be applied as a sensitive temperature sensor based on the emission color change. On the upside the emission intensity variation of **4** has a good response at the low temperature range (up to 100 K) but, nevertheless, the sensitivity at ambient temperature is low (see inset of Fig. S29 in ESI†).

4. Conclusions

In this work, we report the preparation of a new isotypical series of layered LnOFs, formulated as $[Ln(H_3tftp)(H_2O)]$ [where $Ln^{3+} = La^{3+}$ (**1**), $(La_{0.95}Eu_{0.05})^{3+}$ (**2**), $(La_{0.95}Tb_{0.05})^{3+}$ (**3**)] and $(La_{0.94}Eu_{0.03}Tb_{0.03})^{3+}$ (**4**)] from the reaction between lanthanide chloride hydrated salts with the novel organic ligand ((2,4,6-trifluorobenzene-1,3,5-triyl)tris(methylene)) triphosphonic acid (H_6tftp) under hydrothermal conditions. All materials were characterized by using in tandem several standard solid-state techniques. The tripodal H_6tftp organic linker was carefully designed to be used as a primary building unit in the preparation of novel fluorinated LnOFs. H_6tftp and its intermediates were readily prepared in large amounts.

The use of conventional hydrothermal synthesis with the same synthetic conditions (temperature, 180 °C; time, 3 days; water as reaction medium) as for the previously-reported 3D LnOF materials[15e] prepared using the analogue non-fluorinated (benzene-1,3,5-triyl(methylene))triphosphonic acid (H_6bmt), led to a completely distinct structure. While the materials with residues of H_6bmt are 3D structures, the isotypical series herein reported is instead composed of a two-dimensional $_\infty{}^2[La(H_3tftp)(H_2O)]$ neutral coordination polymer, with the hydrophobic aromatic rings pointing to the interlamellar space, and the phosphonate groups and metal centers forming an internal inorganic sheet. It was also found that the fluorinated materials exhibit a much more limited thermal stability upon release of the coordinated water molecules: indeed, while dehydration of the previously-reported 3D materials promotes very small modifications in the LnOF structures, in the $[Ln(H_3tftp)(H_2O)]$ materials a drastic loss of crystallinity was observed instead.

Mixed-lanthanide materials with stoichiometric amounts of optically-active lanthanides have been studied with results unequivocally showing that the presence of the O–H vibrations of the coordinated water molecules, comprising the first coordination sphere, quench the photoluminescence of compounds **2** and **3**. In addition, it was demonstrated that for the materials herein reported the ligand-to-metal charge transfer mechanism is poorly efficient, with the combination of these two factors leading to low absolute emission quantum yields. In this way we are currently investigating in our laboratories synthetic ways to produce new LnOF materials using the novel ligand herein reported without water molecules in the first coordination sphere. With this on-going work we intend to isolate more efficient photoluminescent

materials aimed at their use for the construction of potential sensing devices. Besides changing the reaction parameters (such as temperature, reaction time, solvent, amongst others) we are also looking into other heating methods such as microwave heating and one-pot reactions, which further have the advantage of allowing a faster and low energy-consuming synthetic process (two attractive features to industry).[15d,30]

Acknowledgements

We would like to thank *Fundação para a Ciência e a Tecnologia* (FCT, Portugal), the European Union, QREN, FEDER, COMPETE and *Laboratório Associado Centro de Investigação em Materiais Cerâmicos e Compósitos*, CICECO (Pest C-CTM/LA0011/2013), the research unit QOPNA (PEst-C/QUI/UI0062/2013) for their general funding scheme. We further wish to thank FCT for the R&D project PTDC/QUI-QUI/098098/2008 (FCOMP-01-0124-FEDER-010785), and for specific funding towards the purchase of single-crystal diffractometer. We are also grateful to FCT for the PhD grant No. SFRH/BD/66371/2009 (to SMFV) and the post-doctoral grant SFRH/BPD/63736/2009 (to JAF). We also wish to thank Patrícia Silva (CICECO, Dept. of Chemistry) for help with the electron microscopy EDS mapping studies.

References

1 (*a*) G. Férey, *Chem. Soc. Rev.*, 2008, **37**, 191–214; (*b*) S. Kitagawa, R. Kitaura and S. Noro, *Angew. Chem., Int. Ed.*, 2004, **43**, 2334–2375; (*c*) O. M. Yaghi, M. O'Keeffe, N. W. Ockwig, H. K. Chae, M. Eddaoudi and J. Kim, *Nature*, 2003, **423**, 705–714; (*d*) T. R. Cook, Y. R. Zheng and P. J. Stang, *Chem. Rev.*, 2013, **113**, 734–777; (*e*) N. Stock and S. Biswas, *Chem. Rev.*, 2012, **112**, 933–969.

2 (*a*) D.-X. Xue, A. J. Cairns, Y. Belmabkhout, L. Wojtas, Y. Liu, M. H. Alkordi and M. Eddaoudi, *J. Am. Chem. Soc.*, 2013, **135**, 7660–7667; (*b*) Y. Peng, G. Srinivas, C. E. Wilmer, I. Eryazici, R. Q. Snurr, J. T. Hupp, T. Yildirim and O. K. Farha, *Chem. Commun.*, 2013, **49**, 2992–2994; (*c*) V. Colombo, C. Montoro, A. Maspero, G. Palmisano, N. Masciocchi, S. Galli, E. Barea and J. A. R. Navarro, *J. Am. Chem. Soc.*, 2012, **134**, 12830–12843; (*d*) X. Duan, J. C. Yu, J. F. Cai, Y. B. He, C. D. Wu, W. Zhou, T. Yildirim, Z. J. Zhang, S. C. Xiang, M. O'Keeffe, B. L. Chen and G. D. Qian, *Chem. Commun.*, 2013, **49**, 2043–2045; (*e*) S. H. Yang, X. Lin, W. Lewis, M. Suyetin, E. Bichoutskaia, J. E. Parker, C. C. Tang, D. R. Allan, P. J. Rizkallah, P. Hubberstey, N. R. Champness, K. M. Thomas, A. J. Blake and M. Schröder, *Nat. Mater.*, 2012, **11**, 710–716; (*f*) Y. S. Bae, C. Y. Lee, K. C. Kim, O. K. Farha, P. Nickias, J. T. Hupp, S. T. Nguyen and R. Q. Snurr, *Angew. Chem., Int. Ed.*, 2012, **51**, 1857–1860; (*g*) T. K. Maji, R. Matsuda and S. Kitagawa, *Nat. Mater.*, 2007, **6**, 142–148.

3 (*a*) S. R. Miller, G. M. Pearce, P. A. Wright, F. Bonino, S. Chavan, S. Bordiga, I. Margiolaki, N. Guillou, G. Férey, S. Bourrelly and P. L. Llewellyn, *J. Am. Chem. Soc.*, 2008, **130**, 15967–15981; (*b*) M. Plabst, L. B. McCusker and T. Bein, *J. Am. Chem. Soc.*, 2009, **131**, 18112–18118.

4 (*a*) R. Srirambalaji, S. Hong, R. Natarajan, M. Yoon, R. Hota, Y. Kim, Y. H. Ko and K. Kim, *Chem. Commun.*, 2012, **48**, 11650–11652; (*b*) P. Y. Wu, J. Wang, Y. M. Li, C. He, Z. Xie and C. Y. Duan, *Adv. Funct. Mater.*, 2011, **21**, 2788–2794; (*c*) A. Corma, H. Garcia and F. Xamena, *Chem. Rev.*, 2010, **110**, 4606–4655; (*d*) K. S. Jeong, Y. B. Go, S. M. Shin, S. J. Lee, J. Kim, O. M. Yaghi and N. Jeong, *Chem. Sci.*, 2011, **2**, 877–882.

5 (*a*) D. Maspoch, D. Ruiz-Molina, K. Wurst, N. Domingo, M. Cavallini, F. Biscarini, J. Tejada, C. Rovira and J. Veciana, *Nat. Mater.*, 2003, **2**, 190–195; (*b*) E. Coronado and G. M. Espallargas, *Chem. Soc. Rev.*, 2013, **42**, 1525–1539; (*c*) Y. C. Chuang, W. L. Ho, C. F. Sheu, G. H. Lee and Y. Wang, *Chem. Commun.*, 2012, **48**, 10769–10771.

6 (*a*) Y. Takashima, V. M. Martinez, S. Furukawa, M. Kondo, S. Shimomura, H. Uehara, M. Nakahama, K. Sugimoto and S. Kitagawa, *Nat. Commun.*, 2011, **2**, 168; (*b*) Y. Li, S. S. Zhang and D. T. Song, *Angew. Chem., Int. Ed.*, 2013, **52**, 710–713; (*c*) J. Rocha, L. D. Carlos, F. A. A. Paz and D. Ananias, *Chem. Soc. Rev.*, 2011, **40**, 926–940.

7 (*a*) D. M. Liu, R. C. Huxford and W. B. Lin, *Angew. Chem., Int. Ed.*, 2011, **50**, 3696–3700; (*b*) K. E. deKrafft, W. S. Boyle, L. M. Burk, O. Z. Zhou and W. B. Lin, *J. Mater. Chem.*, 2012, **22**, 18139–18144; (*c*) G. A. Pereira, J. A. Peters, F. A. A. Paz, J. Rocha and C. Geraldes, *Inorg. Chem.*, 2010, **49**, 2969–2974.

8 (*a*) C. Serre, *Angew. Chem., Int. Ed.*, 2012, **51**, 6048–6050; (*b*) T. J. Wu, L. J. Shen, M. Luebbers, C. H. Hu, Q. M. Chen, Z. Ni and R. I. Masel, *Chem. Commun.*, 2010, **46**, 6120–6122; (*c*) C. Yang, U. Kaipa, Q. Z. Mather, X. P. Wang, V. Nesterov, A. F. Venero and M. A. Omary, *J. Am. Chem. Soc.*, 2011, **133**, 18094–18097.

9 (*a*) P. Pachfule, C. Dey, T. Panda and R. Banerjee, *CrystEngComm*, 2010, **12**, 1600–1609; (*b*) Z. H. Zhang, S. C. Chen, J. L. Mi, M. Y. He, Q. Chen and M. Du, *Chem. Commun.*, 2010, **46**, 8427–8429.

10 (*a*) Z. Hulvey, D. A. Sava, J. Eckert and A. K. Cheetham, *Inorg. Chem.*, 2011, **50**, 403–405; (*b*) C. A. Fernandez, P. K. Thallapally, R. K. Motkuri, S. K. Nune, J. C. Sumrak, J. Tian and J. Liu, *Cryst. Growth Des.*, 2010, **10**, 1037–1039; (*c*) S. Biswas, T. Remy, S. Couck, D. Denysenko, G. Rampelberg, J. F. M. Denayer, D. Volkmer, C. Detavernier and P. Van Der Voort, *Phys. Chem. Chem. Phys.*, 2013, **15**, 3552–3561.

11 (*a*) B. L. Chen, Y. Yang, F. Zapata, G. D. Qian, Y. S. Luo, J. H. Zhang and E. B. Lobkovsky, *Inorg. Chem.*, 2006, **45**, 8882–8886; (*b*) B. V. Harbuzaru, A. Corma, F. Rey, P. Atienzar, J. L. Jordá, H. Garcia, D. Ananias, L. D. Carlos and J. Rocha, *Angew. Chem., Int. Ed.*, 2008, **47**, 1080–1083.

12 (*a*) C. Yang, X. P. Wang and M. A. Omary, *J. Am. Chem. Soc.*, 2007, **129**, 15454–15455; (*b*) C. Yang, X. P. Wang and M. A. Omary, *Angew. Chem., Int. Ed.*, 2009, **48**, 2500–2505.

13 (*a*) P. Pachfule, Y. F. Chen, J. W. Jiang and R. Banerjee, *Chem.–Eur. J.*, 2012, **18**, 688–694; (*b*) P. Pachfule, Y. F. Chen,

S. C. Sahoo, J. W. Jiang and R. Banerjee, *Chem. Mater.*, 2011, **23**, 2908–2916.

14 (*a*) J. C. G. Bunzli and S. V. Eliseeva, *Chem. Sci.*, 2013, **4**, 1939–1949; (*b*) J. C. G. Bunzli and C. Piguet, *Chem. Soc. Rev.*, 2005, **34**, 1048–1077; (*c*) S. V. Eliseeva and J. C. G. Bunzli, *New J. Chem.*, 2011, **35**, 1165–1176.

15 (*a*) L. Cunha-Silva, L. Mafra, D. Ananias, L. D. Carlos, J. Rocha and F. A. A. Paz, *Chem. Mater.*, 2007, **19**, 3527–3538; (*b*) F. N. Shi, T. Trindade, J. Rocha and F. A. A. Paz, *Cryst. Growth Des.*, 2008, **8**, 3917–3920; (*c*) P. Silva, F. Vieira, A. C. Gomes, D. Ananias, J. A. Fernandes, S. M. Bruno, R. Soares, A. A. Valente, J. Rocha and F. A. A. Paz, *J. Am. Chem. Soc.*, 2011, **133**, 15120–15138; (*d*) S. M. F. Vilela, A. D. G. Firmino, R. F. Mendes, J. A. Fernandes, D. Ananias, A. A. Valente, H. Ott, L. D. Carlos, J. Rocha, J. P. C. Tomé and F. A. Almeida Paz, *Chem. Commun.*, 2013, **49**, 6400–6402; (*e*) S. M. F. Vilela, D. Ananias, A. C. Gomes, A. A. Valente, L. D. Carlos, J. A. S. Cavaleiro, J. Rocha, J. P. C. Tome and F. A. A. Paz, *J. Mater. Chem.*, 2012, **22**, 18354–18371.

16 F. A. A. Paz, J. Klinowski, S. M. F. Vilela, J. P. C. Tomé, J. A. S. Cavaleiro and J. Rocha, *Chem. Soc. Rev.*, 2012, **41**, 1088–1110.

17 T. Kottke and D. Stalke, *J. Appl. Crystallogr.*, 1993, **26**, 615–619.

18 *APEX2, Data Collection Software Version 2.1-RC13*, Bruker AXS, Delft, The Netherlands, 2006.

19 *Cryopad, Remote monitoring and control, Version 1.451*, Oxford Cryosystems, Oxford, United Kingdom, 2006.

20 *SAINT+, Data Integration Engine v. 7.23a* ©, Bruker AXS, Madison, Wisconsin, USA, 1997–2005.

21 G. M. Sheldrick, *SADABS v.2.01, Bruker/Siemens Area Detector Absorption Correction Program*, Bruker AXS, Madison, Wisconsin, USA, 1998.

22 (*a*) G. M. Sheldrick, *SHELXS-97, Program for Crystal Structure Solution*, University of Göttingen, 1997; (*b*) G. M. Sheldrick, *Acta Crystallogr., Sect. A: Found. Crystallogr.*, 2008, **64**, 112–122.

23 G. M. Sheldrick, *SHELXL-97, Program for Crystal Structure Refinement*, University of Göttingen, 1997.

24 K. Brandenburg, *Diamond, Version 3.2. Crystal Impact GbR*, Bonn, Germany, 2009.

25 C. F. Macrae, I. J. Bruno, J. A. Chisholm, P. R. Edgington, P. McCabe, E. Pidcock, L. Rodrigues-Monge, R. Taylor, J. van de Streek and P. A. Wood, *J. Appl. Crystallogr.*, 2008, **41**, 466–470.

26 S. Samai and K. Biradha, *CrystEngComm*, 2009, **11**, 482–492.

27 E. V. Alexandrov, V. A. Blatov, A. V. Kochetkov and D. M. Proserpio, *CrystEngComm*, 2011, **13**, 3947–3958.

28 V. A. Blatov, *Struct. Chem.*, 2012, **23**, 955–963, http://www.topos.samsu.ru.

29 G. Socrates, *Infrared Characteristic Group Frequencies: Tables and Charts*, 2nd edn, John Wiley & Sons Ltd, Baffins Lane, Chichester, 1994.

30 S. M. F. Vilela, R. F. Mendes, P. Silva, J. A. Fernandes, J. P. C. Tome and F. A. A. Paz, *Cryst. Growth Des.*, 2013, **13**, 543–560.

